Thermodynamics of polymer/diluent systems for thermally induced phase separation: 3. Liquid–liquid phase separation systems

Sung Soo Kim and Douglas R. Lloyd*
Department of Chemical Engineering, Centre for Polymer Research, The University of Texas at Austin, Austin, TX 78712, USA
(Received 7 January 1991; accepted 30 March 1991)

Thermodynamic analysis of the system isotactic polypropylene/n,n-bis(2-hydroxyethyl) tallowamine was performed using Flory's equation of state theory adapted to the polymer/oligomer system using parameters determined in the first paper in this series. The estimated results were in good agreement with those from melting temperature depression and cloud point measurements. The equilibrium phase diagram was estimated even in the experimentally unavailable region. When the estimated phase diagram could be compared with the experimental data, the agreement was good. The interaction parameter for this system increased greatly with temperature resulting in upper critical solution temperature behaviour. The increased end group polarity of n,n-bis(2-hydroxyethyl) tallowamine resulted in much greater enthalpic interactions than the n-alkane and n-fatty acid systems covered in the second paper in this series.

(Keywords: interaction parameter; phase separation; equation of state)

INTRODUCTION

In a previous paper in this series, thermodynamic analysis of solid–liquid thermally induced phase separation (TIPS) via polymer crystallization was performed using Flory's equation of state (EOS) theory adapted for polymer/oligomer systems[1]. Liquid–liquid TIPS for semicrystalline polymer/diluent systems is more complicated in terms of thermodynamics and phase separation kinetics than solid–liquid TIPS. Coexistence of liquid–liquid and solid–liquid phase separation curves must be considered for proper interpretation of TIPS membrane formation[2–7]. TIPS behaviour depends on the shape of the phase diagram and the sequence of phase separation events under certain cooling conditions[4], both of which can be represented on the phase diagram. Therefore, thermodynamic analysis, especially interaction parameter estimation, is helpful in understanding TIPS. Knowledge of the interaction parameter at various temperatures and compositions is essential for the estimation of the phase diagram, especially in regions of the phase diagram that are experimentally inaccessible. The driving force for solid–liquid and liquid–liquid TIPS can be specified to give a basis for kinetic studies of phase separation and to help understand the phase separation behaviour as well as the resulting membrane structure. To do so the interaction parameter should be estimable at any point on the phase diagram.

In this paper, isotactic polypropylene (iPP)/n,n-bis-(2-hydroxyethyl) tallowamine (TA) was selected as a model liquid–liquid phase separation system because it is currently used to prepare commercially available membranes[8]. The formula of TA is CH_3–$(CH_2)_{16-18}$–N = $(CH_2OH)_2$, which is similar to the n-alkanes and n-fatty acids reported earlier[1] except for the end group. Since the TA end group is more polar than those of the other diluents studied in reference 1, enthalpic interactions are expected to be unfavourably strong and cause system instability.

A knowledge of how the interaction parameter varies with temperature and composition is necessary to predict the TIPS behaviour. Therefore, a primary objective of this paper was to estimate this information using Flory's EOS theory adapted to the polymer/oligomeric diluent system, and compare the results to experimental data from cloud point and melting temperature depression measurements. Having generated the interaction parameter data, a second objective was to estimate equilibrium melting temperatures as well as binodal and spinodal points to construct the iPP/TA phase diagram. To validate the predicted phase diagram, it was compared with the experimentally generated data. System stability was tested to examine the miscibility of the system. The results obtained in this series of papers gave background for the structural study performed by the authors[2–7].

The basic thermodynamic equations and experimental procedures were introduced in previous papers in this series[1,9].

THERMODYNAMICS OF LIQUID–LIQUID PHASE SEPARATION

Liquid–liquid phase separation takes place if the system does not satisfy all of the following stability conditions[10].

$$\Delta G^1/RT < 0 \quad (1)$$

$$[\partial^2(\Delta G^1/RT)/\partial\phi_2^2]_{P,T} > 0 \quad (2)$$

* To whom correspondence should be addressed

0032-3861/92/051047-11

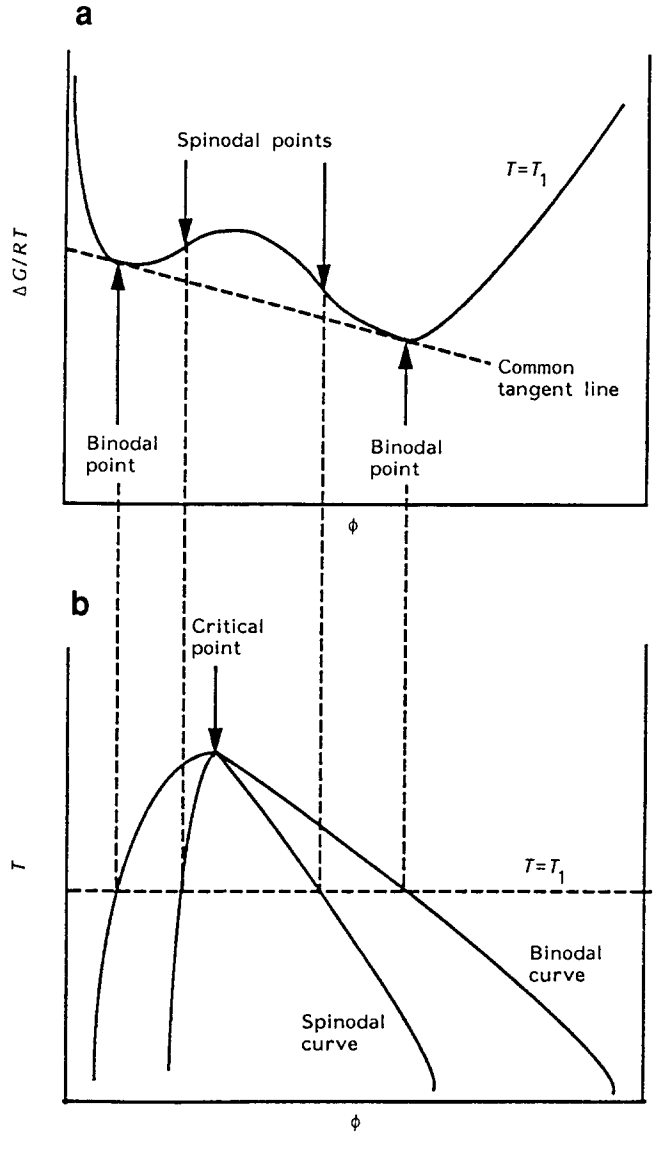

Figure 1 Schematic plot of liquid–liquid phase separation: (a) Gibbs free energy of mixing as a function of polymer volume fraction; (b) temperature *versus* polymer volume fraction

The nomenclature used in this paper was introduced in references 1 and 9.

As shown in *Figure 1a* at the spinodal points (ϕ'_{2s} and ϕ''_{2s}) equation (3) is satisfied at a certain temperature ($T = T_1$)[11]:

$$[\partial^2(\Delta G^1/RT)/\partial\phi_2^2]_{P,T} = 0 \qquad (3)$$

The spinodal points at various temperatures make a locus called a spinodal curve (*Figure 1b*). Below the spinodal curve, the system does not satisfy equation (2). The system is unstable and there is a spontaneous liquid–liquid phase separation simultaneously everywhere in the system, which is called spinodal decomposition[12–14].

If a common tangent line is drawn on the $\Delta G^1/RT$ *versus* ϕ_2 plot, as shown in *Figure 1a*, the co-tangential points are called binodal points (ϕ'_{2b} and at ϕ''_{2b}). At the binodal points at $T = T_1$, equations (4) and (5) must be satisfied[13].

$$[\partial(\Delta G^1/RT)/\partial\phi_2] \text{ at } \phi'_{2b} = [\partial(\Delta G^1/RT)/\partial\phi_2] \text{ at } \phi''_{2b} \qquad (4)$$

$$\{(\Delta G^1/RT) - [\partial(\Delta G^1/RT)/\partial\phi_2]\phi_2\} \text{ at } \phi'_{2b} = \{(\Delta G^1/RT) - [\partial(\Delta G^1/RT)/\partial\phi_2]\phi_2\} \text{ at } \phi''_{2b} \qquad (5)$$

The locus of the binodal points at various temperatures makes a binodal curve, as shown in *Figure 1b*. The region between the spinodal and binodal curves is called the metastable region. There is no spontaneous liquid–liquid phase separation in this region, since the system is stable to small concentration fluctuations. Liquid–liquid phase separation takes place only at points where there is a large concentration fluctuation[13]. The phase separated domain grows by diffusion of diluent down the concentration gradient. This two-stage process is called nucleation and growth[14,15].

In *Figure 1b* there is a critical point, where the binodal and spinodal curves coincide and equations (6) and (7) are satisfied

$$\partial(\Delta\mu_2^R/RT)/\partial\phi_2 = 1/(r_2\phi_2) - (1/r_2 - 1/r_1) - 2\chi_{\mu 2}(1 - \phi_2) = 0 \qquad (6)$$

$$\partial^2(\Delta\mu_2^R/RT)/\partial\phi_2^2 = -1/(r_2\phi_2^2) + 2\chi_{\mu 2} = 0 \qquad (7)$$

The critical composition (ϕ_{2c}) and the critical interaction parameter ($\chi_{\mu 2c}$) can be obtained by solving simultaneously equations (6) and (7). If the composition dependence of the interaction parameter is neglected, ϕ_{2c} and $\chi_{\mu 2c}$ are functions of r_1 and r_2 only[11,16]. $\chi_{\mu 2c}$ can be used as a criterion for system miscibility.

In the second paper in this series[1], $\Delta G^1/RT$ and its first and second derivatives were expressed in terms of EOS parameters, where the composition dependence of the interaction parameter is considered. The Gibbs free energy of mixing per lattice site can be expressed as the sum of the combinatorial terms per lattice site, residual entropy change of mixing per lattice site (S^{R1}) and the residual enthalpy change of mixing per lattice site (H^{R1}).

$$\Delta G^1/RT = (\phi_1/r_1)\ln(\phi_1) + (\phi_2/r_2)\ln(\phi_2) - S^{R1}/R + H^{R1}/RT \qquad (8)$$

The residual entropy and enthalpy change of mixing per lattice site were obtained from Flory's EOS theory[1].

$$S^{R1} = -3(V_2^*/r_2)\{\phi_1(P_1^*/T_1^*)\ln[(\tilde{V}_1^{1/3} - 1)/(\tilde{V}^{1/3} - 1)] + \phi_2(P_2^*/T_2^*)\ln[(\tilde{V}_2^{1/3} - 1)/(\tilde{V}^{1/3} - 1)]\} \qquad (9)$$

$$H^{R1} = (V_2^*/r_2)\{\phi_1 P_1^*(\tilde{V}_1^{-1} - \tilde{V}^{-1}) + \phi_2 P_2^*(\tilde{V}_2^{-1} - \tilde{V}^{-1}) + [(\phi_1\theta_2)(X_{12}/\tilde{V})]\} \qquad (10)$$

Since the interaction parameter obtained from the experimental data is based on the chemical potential equation of the polymer ($\chi_{\mu 2}$)[17], all the thermodynamic functions in this study are expressed in terms of $\chi_{\mu 2}$. Then, the first derivative of $\Delta G^1/RT$ can be expressed as

$$\partial(\Delta G^1/RT)/\partial\phi_2 = -\ln(\phi_1)/r_1 + \ln(\phi_2)/r_2 + (1/r_2 - 1/r_1) + \chi_{\mu 2}(\phi_1 - \phi_2) \qquad (11)$$

$\chi_{\mu 2}$ was derived by Flory from the partial molar residual enthalpy ($\bar{H}_2^R$) and entropy ($\bar{S}_2^R$) of the polymer[1,17]:

$$\chi_{\mu 2} = (\bar{H}_2^R - T\bar{S}_2^R)/(RTr_2\phi_1^2) = (P_2^*V_2^*/RTr_2\phi_1^2)\{3\tilde{T}_2\ln[(\tilde{V}_2^{1/3} - 1)/(\tilde{V}^{1/3} - 1)] + (\tilde{V}_2^{-1} - \tilde{V}^{-1})\} + (V_2^*/RTr_2\phi_2^2)(\theta_2^2 X_{12}/\tilde{V}) \qquad (12)$$

The interaction parameter based on the chemical potential equation of diluent ($\chi_{\mu 1}$) was also derived.

$$\chi_{\mu 1} = (\bar{H}_1^R - T\bar{S}_1^R)/(RTr_1\phi_2^2)$$
$$= (P_1^*V_1^*/RTr_1\phi_2^2)\{3\tilde{T}_1 \ln[(\tilde{V}_1^{1/3} - 1)/(\tilde{V}^{1/3} - 1)] + (\tilde{V}_1^{-1} - \tilde{V}^{-1})\} + (V_1^*/RTr_1\phi_2^2)(\theta_2^2 X_{12}/\tilde{V}) \quad (13)$$

The second derivative of $\Delta G^1/RT$ is expressed as:

$$\partial^2(\Delta G^1/RT)/\partial\phi_2^2 = 1/(r_1\phi_1) + 1/(r_2\phi_2) - 2\chi_{\mu 2} + (\phi_1 - \phi_2)\partial\chi_{\mu 2}/\partial\phi_2 \quad (14)$$

where $\partial\chi_{\mu 2}/\partial\phi_2$ can be obtained from the following equation

$$\partial\chi_{\mu 2}/\partial\phi_2 = \{[\partial(\Delta\mu_2^R/RT)/\partial\phi_2] + 2r_2\phi_1\chi_{\mu 2}\}/r_2\phi_1^2 \quad (15)$$

A derivative of the residual chemical potential in terms of ϕ_2 was obtained as

$$\partial(\Delta\mu_2^R/RT)/\partial\phi_2 = (P_2^*V_2^*/RT_2^*) \times [-(d\tilde{V}/d\phi_2)/(\tilde{V} - \tilde{V}^{2/3})] + [P_2^*V_2^*(d\tilde{V}/d\phi_2)/RT\tilde{V}^2] - [(2V_2^*/RT)(X_{12}/\tilde{V})(\theta_2/\phi_2)^3\phi_1] - [V_2^*X_{12}(d\tilde{V}/d\phi_2)(\theta_2^2/RT\tilde{V}^2)(\phi_1/\phi_2)^2] \quad (16)$$

The derivatives of reduced parameters in equation (16) were obtained according to Sham and Walsh's method as introduced in references 1, 18 and 19.

PHASE DIAGRAM DETERMINATION

iPP was supplied by Himont Co. (Profax 6723, lot no. 79316) and TA was purchased from Armak Chemicals (Armostat 310). Homogeneous iPP/TA mixtures were prepared in test tubes. Measured amounts of iPP and TA were charged to the test tube and purged with N_2 for 2 min to prevent oxidation. The test tube was sealed with a flame and put in an oven at 473 K for 24 h. Composition was confirmed by measuring the amount of diluent removed in a Soxhlet apparatus. These samples were used to determine cloud points, crystallization temperatures and equilibrium melting temperatures.

Since the iPP/TA system has a monotectic phase diagram, the system undergoes either solid–liquid phase separation or liquid–liquid phase separation depending on the initial composition. As the temperature is decreased, the iPP/TA mixtures of iPP concentration less than the monotectic composition are expected to become unstable and pass through the binodal curve. Liquid–liquid TIPS takes place and the sample gets cloudy. The experimental liquid–liquid phase separation point is called a cloud point. For iPP concentration greater than the monotectic composition the system is stable and undergoes solid–liquid TIPS via iPP crystallization. The dynamic crystallization temperature and equilibrium melting temperature at each composition were determined using a Perkin–Elmer DSC 7.

Cloud point measurement

A number of analytical methods have been developed to determine the binodal curve for polymer solutions. These methods include light scattering[20–23], pulse-induced critical scattering[24], low-speed centrifugation[25], fluorescence quenching[26,27], n.m.r.[28,29] and optical density measurement[30–33]. The optical density measurement is attractive for the following reasons: it is simple, it is easy to control the temperature of the sample by using a temperature-programmed hot stage and the amount of sample is small and easily prepared.

In this study the optical density of the sample was measured by a thermo-optical microscope (TOM) to determine the cloud point. The TOM apparatus was assembled with a Mettler FP82 hot stage and FP80 central processor, Bausch & Lomb WB6211 microscope, and Spex Co. Minimate light source as shown in *Figure 2*. The TOM apparatus is designed to monitor the transmittance of light through the sample on the hot stage. If the sample underwent liquid–liquid phase separation and became cloudy, the transmittance decreased and the inflection point was taken as the cloud point. The details of the experimental procedure follow.

A thin slice of the polymer/diluent solid sample was obtained. Although a solid homogeneous sample was obtained by the test tube method described above, it was not always possible to maintain the homogeneity on the hot stage. When the mixture sample was placed on the hot stage, the diluent melted and separated from the unmelted iPP. After the sample was held at 473 K for 10 min, it became homogeneous, as reported by Lim[34]. If it was held at 473 K longer than 10 min, the sample might undergo degradation and lose diluent by vaporization. To overcome errors caused by inhomogeneity of the melt sample, the average was taken from more than 20 samples from the same batch. The hot stage parameters were set as: initial temperature, 473 K; cooling rate, 10 K min^{-1}; and final temperature, 373 K.

The sample was placed between a pair of cover slips, which were subsequently sealed along all four edges with Teflon tape and vacuum grease, and placed on a hot stage preset at 473 K. Teflon tape and silicone vacuum grease were applied to the edges of the bottom cover slip before charging the sample between the cover slips for two reasons: first, to seal the two cover slips and prevent diluent loss by vaporization; and second, to help maintain the original sample thickness, which would otherwise be reduced by the weight of the top cover slip.

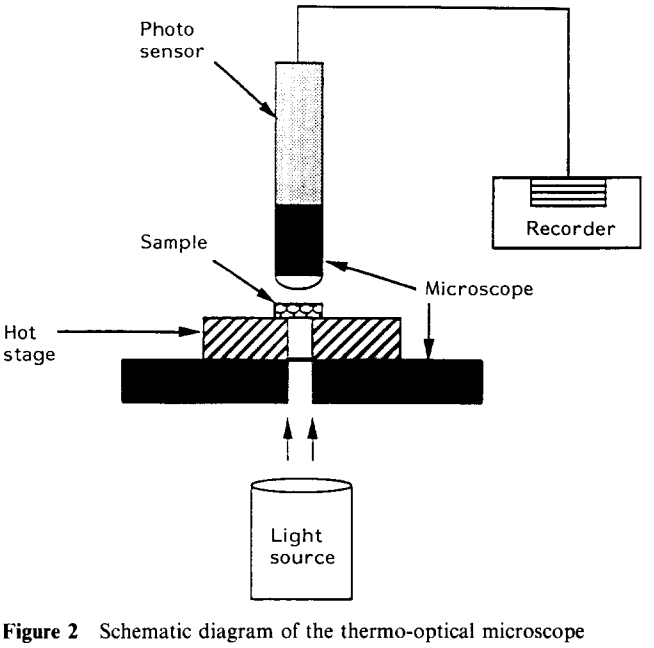

Figure 2 Schematic diagram of the thermo-optical microscope

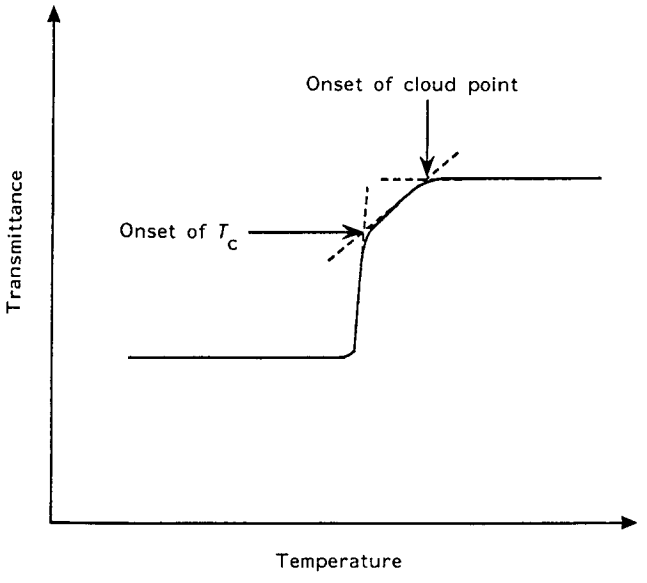

Figure 3 Typical shape of a TOM recording

Since change in sample thickness affects the transmittance of the light through the sample, it is important to maintain a constant sample thickness throughout the measurement period. The sample was held at 473 K for 5 min to make a homogeneous melt and to stabilize the instrument. The light source was turned on and the wavelength was set at 628 nm. A wavelength of 628 nm was selected to maximize the transmittance change at the liquid–liquid phase separation point for the iPP/TA system after a few initial trials. The sample was cooled at 10 K min^{-1} and the transmittance of the light through the sample on the hot stage was recorded.

Since iPP is semicrystalline, the liquid–liquid TIPS was followed by iPP crystallization. The crystallization was also monitored by TOM after the liquid–liquid phase separation. A typical recorded plot of the TOM experiment is shown in *Figure 3*. The onset of the cloud point was defined as the intercept of the extrapolation lines shown in *Figure 3*. As the initial iPP concentration approached the monotectic composition, the cloud point and the crystallization temperature got closer and it became more difficult to distinguish them.

Cloud points for the iPP/TA system measured at a cooling rate of 10 K min^{-1} are plotted in *Figure 4*. Preliminary experiments using cooling rates in the range of 3–20 K min^{-1} yielded nearly the same results with no deviation of >3 K. Therefore, the cloud points measured at 10 K min^{-1} were used to approximate the equilibrium values, and the interaction parameters were calculated from the cloud point data.

Cloud points to the left of the critical point could not be obtained experimentally, since homogeneous samples could not be obtained in this concentration range. When the sample in this concentration range was prepared in a test tube and cooled, the sample underwent liquid–liquid phase separation and the polymer-lean phase formed the continuous phase with a dispersed polymer-rich phase.

Dynamic crystallization temperature measurement

The dynamic crystallization temperature is important in the TIPS process. The location of the crystallization temperature curve depends on the cooling rate due to the supercooling effect. The position of the dynamic monotectic point is affected by the location of the crystallization curve. Dynamic crystallization temperatures were measured by d.s.c. at a cooling rate of 10 K min^{-1}. Initially the sample was heated to 473 K and held for 10 min. The sample was then cooled at 10 K min^{-1}, and the exotherm peak temperature was taken as the crystallization temperature. The crystallization temperatures at 10 K min^{-1} are plotted in *Figure 4*. The intercept of the crystallization curve and the cloud point curve, which is the monotectic point at a cooling rate of 10 K min^{-1} was 380 K and 59 wt% iPP.

The crystallization curve below the cloud point curve is nearly horizontal. This can be explained in terms of the phase separation mechanism. When any sample within the liquid–liquid phase separation range was slowly cooled, it entered the unstable or metastable region and underwent liquid–liquid phase separation to make polymer-rich and polymer-lean phases. If the cooling process was slow enough for the polymer-rich phase to follow the cloud point curve, the sample eventually reached the monotectic point regardless of its initial composition. The crystallization process began at this point and was the same for every sample within this range.

Equilibrium melting temperature determination

Equilibrium melting temperature data are important, since they form an equilibrium solid–liquid phase separation boundary in the phase diagram and the interaction parameter can be calculated from these data[16,35]. The details for determining the equilibrium melting temperatures were covered in the second paper in this series[1]. Hoffman–Weeks plots[36] were used to

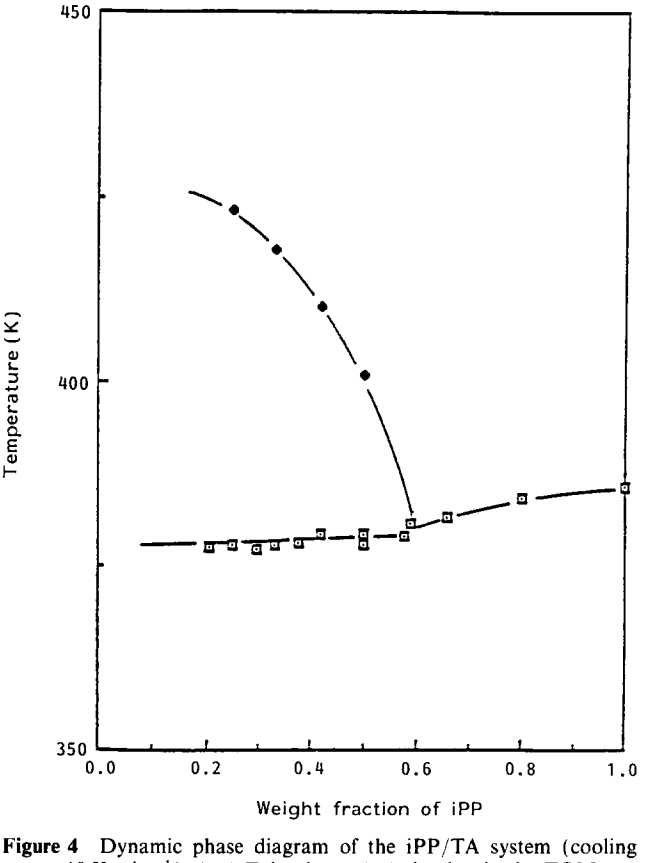

Figure 4 Dynamic phase diagram of the iPP/TA system (cooling rate = 10 K min^{-1}): (□) T_c by d.s.c.; (◆) cloud point by TOM

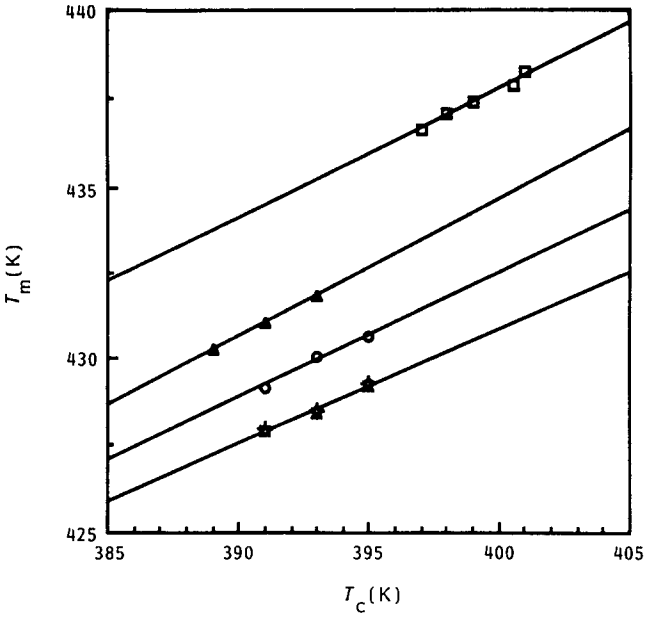

Figure 5 Hoffman–Weeks plot of the iPP/TA system: (□) pure PP; (▲) 90 wt% iPP; (○) 70 wt% iPP; (+) 50 wt% iPP; (×) 33 wt% iPP; (◆) 25 wt% iPP

determine the equilibrium melting temperatures, as shown in *Figure 5*.

The equilibrium melting curve for the iPP/TA system is plotted in *Figure 6*. The equilibrium melting curve is located above the cloud point curve, whereas the dynamic crystallization curve in *Figure 4* coexists with the cloud point curve. That is, as the cooling rate was decreased, the dynamic crystallization curve shifted to higher temperatures. Consequently, the intersection with the invariant cloud point curve (monotectic point) moved to lower polymer concentrations and higher temperatures.

The equilibrium melting curve was also horizontal below 50 wt% iPP. This is shown in *Figure 5*, in which the Hoffman–Weeks plots of samples with 50, 33, and 25 wt% iPP are identical. Theoretically, the equilibrium melting curve must exist as shown by the broken line in *Figure 6* in the concentration range below 50 wt% iPP. The nature of the method used to determine the equilibrium melting temperature did not generate the true equilibrium melting temperatures below an iPP concentration of 50 wt%. For the Hoffman–Weeks plot method, the sample was crystallized at a certain crystallization temperature (T_c)[36]. As shown in *Figure 6*, the T_c range selected for constructing the Hoffman–Weeks plot is located below the cloud point curve for an iPP concentration of < 50 wt% iPP. Therefore, when samples below this concentration were quenched to T_c, they underwent liquid–liquid phase separation prior to iPP crystallization.

EXPERIMENTAL INTERACTION PARAMETER DETERMINATION

Interaction parameter from cloud points

Although the cloud point is an indication of liquid–liquid TIPS, there is still controversy as to whether it is a binodal or a spinodal point. From the results of structural studies[2–7] and the reasoning below, it was concluded that the cloud point is closer to a binodal point than a spinodal point.

When the homogeneous melt sample is cooled slowly to enter the metastable region, only locations with large concentration fluctuations phase separate. If the solution is sufficiently homogeneous to prevent any significant concentration fluctuations and there are no impurities to serve as nuclei, there is no phase separation within the metastable region until the solution reaches the spinodal point. However, a completely homogeneous melt free from impurities is not practically obtainable. Consequently nuclei initiate nucleation and growth within the metastable region and liquid–liquid phase separation is more likely to begin near the binodal point.

Assuming the cloud point represents the binodal point, the interaction parameter was calculated using the EOS method. The conditions at the binodal point were given in equations (4) and (5), and $\chi_{\mu 2}$ was calculated by introducing $\Delta G^1/RT$ and $\partial(\Delta G^1/RT)/\partial\phi_2$ (equations (8)–(12)) into equations (4) and (5). In *Table 1*, calculated $\chi_{\mu 2}$ are listed for each cloud point composition and temperature. These results are compared with the estimated values given later.

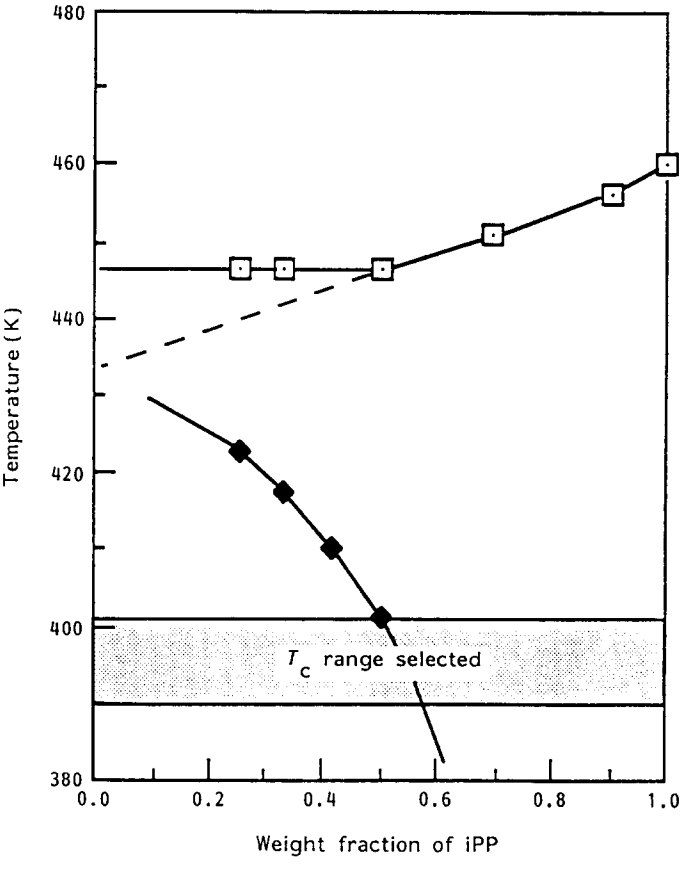

Figure 6 Equilibrium experimental phase diagram of the iPP/TA system: (□) equilibrium T_m; (◆) cloud point

Table 1 Interaction parameter by cloud point measurement iPP/TA system

Temperature (K)	Volume fraction of iPP	$\chi_{\mu 2}$ ($\times 10^2$)	X_{12} (J cm^{-3})
401.0	0.50	10.14	8.10
410.0	0.42	9.24	7.70
417.6	0.33	8.26	7.20
423.0	0.25	7.66	6.83

Interaction parameter from melting temperature depression

The interaction parameter can be obtained from the T_m depression equation[16,35]:

$$[(1/r_1 - 1/r_2)\phi_1 - 1/r_2 \ln \phi_2] - (1/T_m - 1/T_m^0)(\Delta H_{fu}/R) = \chi_{\mu 2}\phi_1^2 \quad (17)$$

where T_m and T_m^0 are the equilibrium melting temperature of the polymer in a mixture and in the pure state, respectively. $\chi_{\mu 2}$ at T_m can be determined from the slope of the linear plot of $[(1/r_1 - 1/r_2)\phi_1 - 1/r_2 \ln \phi_2] - (1/T_m - 1/T_m^0)(\Delta H_{fu}/R)$ *versus* ϕ_1^2, and ΔH_{fu} can be determined from the intercept of the plot assuming a composition-independent interaction parameter.

Since it was revealed that melting temperatures obtained from the Hoffman–Weeks method for iPP concentrations below 50 wt% are not purely thermodynamic, the data for concentrations of >50 wt% iPP were used to calculate the interaction parameter by equation (17). $\chi_{\mu 2}$ for the iPP/TA system was taken from the slope of *Figure 7* as 0.056. $\chi_{\mu 2}$ obtained by this procedure is not a value at a specific composition and corresponding T_m. The procedure is based on the assumption that $\chi_{\mu 2}$ is independent of composition and temperature within the equilibrium T_m range. Therefore, it is reasonable to regard this $\chi_{\mu 2}$ value as that at an iPP volume fraction of 0.75 and the corresponding T_m. The interaction parameter obtained from this method is discussed and compared with the estimated value in the next section.

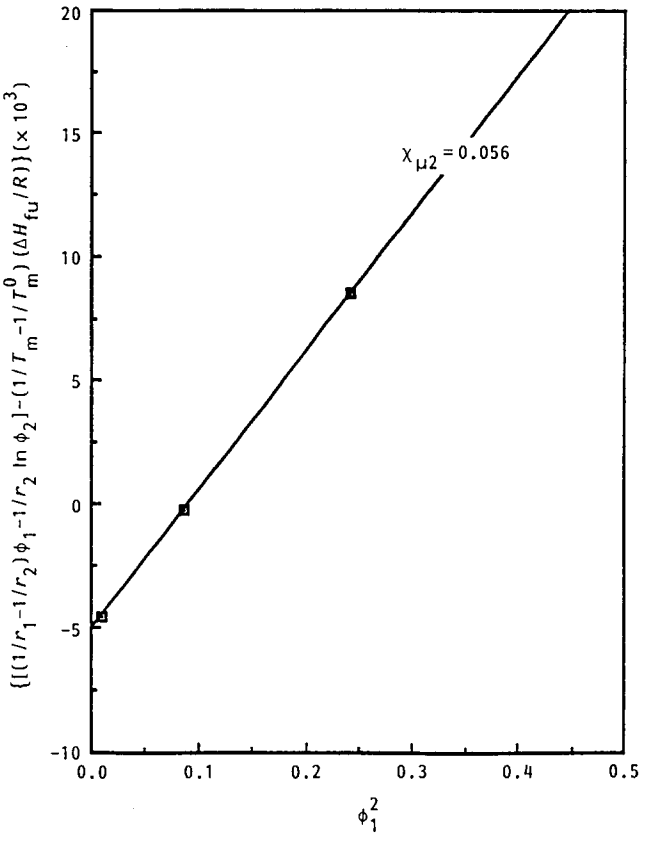

Figure 7 Interaction parameter determination from melting temperature measurement for the iPP/TA system

INTERACTION PARAMETER ESTIMATION BY EOS

Comparison of estimated and experimental interaction parameters

Interaction parameters based on the chemical potential equations of diluent ($\chi_{\mu 1}$) and polymer ($\chi_{\mu 2}$) were obtained from equations (12) and (13) using the EOS parameters obtained[1]. $\chi_{\mu 1}$ and $\chi_{\mu 2}$ are plotted in *Figure 8* at an iPP volume fraction of 0.5. They were compared with the experimental $\chi_{\mu 2}$ values obtained from the cloud point and T_m depression measurement. The experimental interaction parameters were determined at each cloud point composition listed in *Table 1*. The interaction parameter from T_m depression measurement was defined at the iPP volume fraction of 0.75 as discussed above. Hence, there is a discrepancy in the compositions used for the estimated and the experimental interaction parameters in *Figure 8*. However, since there is little composition dependence of the interaction parameter for the iPP/TA system, which is proved later in this paper, comparison of the estimated and experimental interaction parameter is reasonable.

The interaction parameters in *Figure 8*, experimental or estimated, decreased with increasing temperature, since enthalpic interactions are dominant for this system. However, the rate of decrease for the experimental data is greater than for the estimated data. The experimental $\chi_{\mu 2}$ intersect with estimated $\chi_{\mu 2}$ at 420 K. Below 420 K it was underestimated and above 420 K it was overestimated.

Underestimation of $\chi_{\mu 2}$ can be attributed to deviation in the extrapolation of the X_{12} parameter to the polymeric system in Figure 10 in the first paper in this series[9]. Overestimation of $\chi_{\mu 2}$ might be caused by the

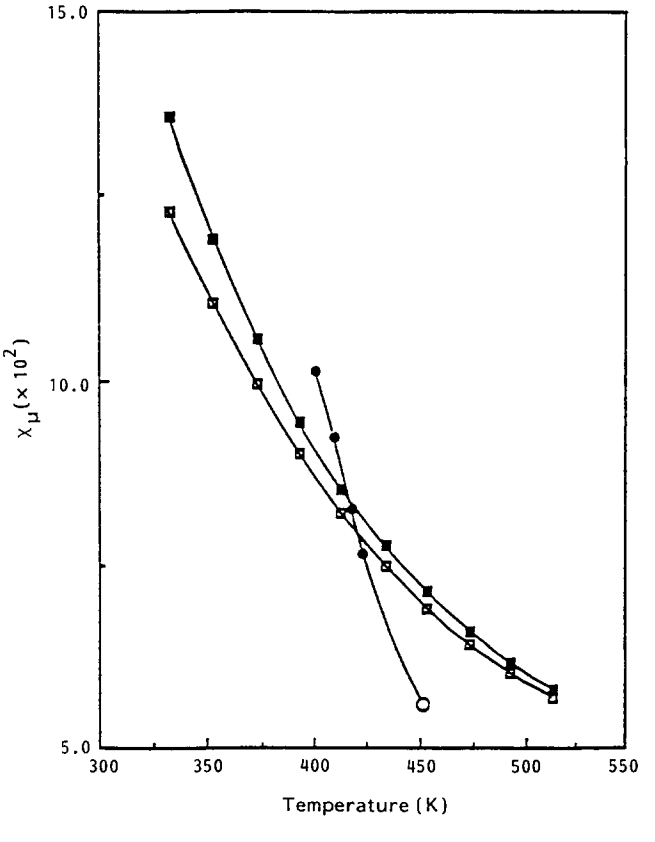

Figure 8 Interaction parameter estimation by EOS and comparison with experimental data for the iPP/TA system (volume fraction of iPP = 0.5 for EOS estimation): (□) $\chi_{\mu 1}$ from EOS; (■) $\chi_{\mu 2}$ from EOS; (●) $\chi_{\mu 2}$ from cloud point; (○) $\chi_{\mu 2}$ from T_m depression

temperature dependence of the X_{12} parameter, which is contrary to the assumption made in the first paper in this series[9]. As shown in *Table 1*, the X_{12} parameter decreases with increasing temperature, if the estimated $\chi_{\mu 2}$ values were forced to coincide with the experimental data by adjusting the X_{12} parameter. The temperature dependence of the X_{12} parameter is explained below in terms of hydrogen bonding for the iPP/TA system.

The enthalpic interaction between iPP and TA is repulsive, since iPP is non-polar and TA is polar. Some of the polarity of TA is due to hydrogen bonding between TA molecules, which results in self association of TA molecules at low temperatures[37]. The self association of TA increased X_{12}, since it increased the η_{11} value in its definition.

$$X_{12} = s_1(\eta_{11} + \eta_{22} - 2\eta_{12})/(2v^{*2}) \qquad (18)$$

where s_1 is the number of contact sites per diluent segment, η_{ij} is the energy parameter for the ij segment pair, and v^* is the specific core volume of the mixture[38]. The assumption of constant X_{12} with temperature was based on the fact that although each η_{ij} parameter changed with temperature, the difference remained constant[39]. However, as illustrated by Coleman *et al.* the equilibrium constant of association by hydrogen bonding is reduced and thereby the hydrogen bonding effect is decreased by increasing the temperature[37,40–43]. This decrease of hydrogen bonding with increasing temperature must be reflected more in η_{11} than the other η_{ij}; consequently, there is a decrease in X_{12}.

It was impossible to collect more X_{12} data below 401 K, since the cloud points were not measurable below that temperature. The X_{12} values at temperatures lower than 420 K were greater than the value obtained from the heat of mixing for analogous systems and extrapolated to the polymeric system (7.200 J cm^{-3}). Therefore, it is impossible to examine the temperature dependence of the X_{12} parameter for a wider temperature range than that of *Figure 8*.

There must also be hydrogen bonding and a temperature dependence of X_{12} in iPP/n-fatty acid systems. The hydrogen bonding effect for iPP/n-fatty acid systems is not as significant as that of the iPP/TA system, since the number of sites for hydrogen bonding per n-fatty acid molecule is smaller than that per TA molecule. X_{12} parameters for iPP/n-fatty acid systems (2.766 J cm^{-3} for iPP/$C_{14}H_{29}COOH$ and 2.128 J cm^{-3} for iPP/$C_{19}H_{39}COOH$) are much smaller than for the iPP/TA system (7.200 J cm^{-3}), partly because of less hydrogen bonding effect in the iPP/n-fatty acid systems. The absolute values of X_{12} for the iPP/n-fatty acid systems are relatively small; therefore, X_{12} tolerates the errors induced by ignoring temperature dependence, since the magnitude of the absolute change of X_{12} may be related to the magnitude of its absolute value.

Contributions of enthalpic and entropic interaction parameters

Variation of the interaction parameter and its entropic ($\chi_{\mu 2s}$) and enthalpic ($\chi_{\mu 2h}$) contributions with temperature were examined at the critical composition. $\chi_{\mu 2s}$ and $\chi_{\mu 2h}$ were estimated from the partial molar residual entropy ($\bar{S}_2^R$) and the partial molar residual enthalpy ($\bar{H}_2^R$) of polymer[1].

$$\chi_{\mu 2s} = -T\bar{S}_2^R/(RTr_1\phi_2^2) \qquad (19)$$

$$\chi_{\mu 2h} = \bar{H}_2^R/(RTr_1\phi_2^2) \qquad (20)$$

The critical composition (ϕ_{2c}) and the critical interaction parameter ($\chi_{\mu 2c}$) were obtained from equations (21) and (22)[11,16].

$$\phi_{2c} = 1/[1 + (r_2/r_1)^{1/2}] \qquad (21)$$

$$\chi_{\mu 2c} = (1/2)(1/r_2^{1/2} + 1/r_1^{1/2})^2 \qquad (22)$$

where r_1, r_2, ϕ_{2c} and $\chi_{\mu 2c}$ for the iPP/TA system are listed in *Table 2* at the critical temperature of the system (429 K). In this study the effect of the molecular weight distribution was ignored for both iPP and TA.

As shown in *Figure 9*, $\chi_{\mu 2h}$ is the dominant contribution to $\chi_{\mu 2}$. $\chi_{\mu 2}$ and $\chi_{\mu 2h}$ drastically decreased with increasing temperature, which is typical of upper critical solution temperature (*UCST*) systems. $\chi_{\mu 2}$ intersects the $\chi_{\mu 2c}$ line at 429 K and this is the *UCST* for the iPP/TA system. Therefore, the system is unstable below 429 K and stable above 429 K at ϕ_{2c}. Liquid–liquid phase separation is expected for this system when the temperature is decreased below the *UCST*. If *Figure 9* is extended to higher temperatures than shown, $\chi_{\mu 2s}$ will continue to increase and becomes the dominant factor, and $\chi_{\mu 2}$ should increase to reach the lower critical solution temperature (*LCST*).

Table 2 Critical composition and critical interaction parameter for iPP/TA

System	Temperature (K)	r_1	ϕ_{2c}	$\chi_{\mu 2c}$	$\chi_{\mu 2}/\chi_{\mu 2c}$
iPP/TA	401.0	7.81	0.080	0.076	1.334

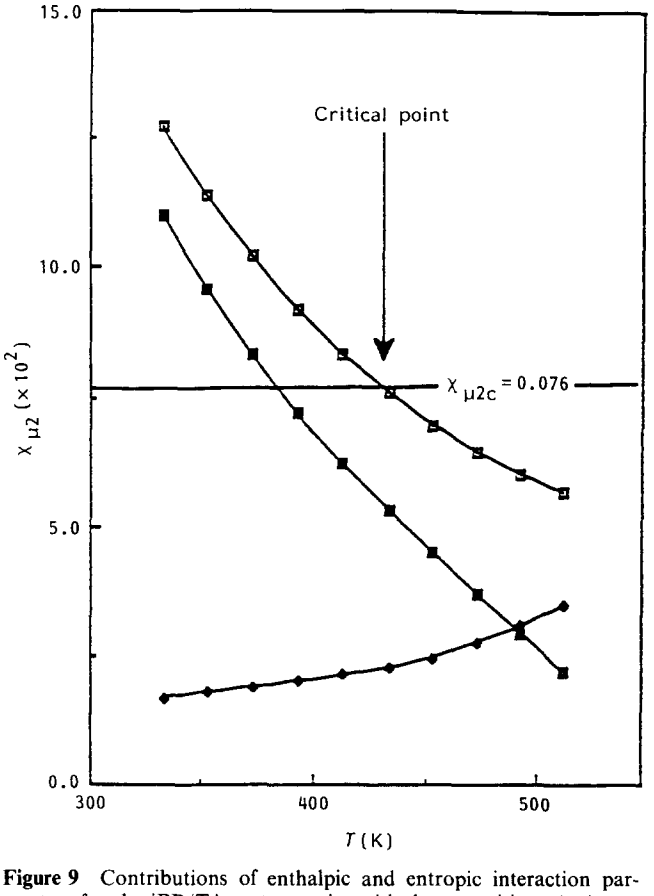

Figure 9 Contributions of enthalpic and entropic interaction parameters for the iPP/TA system at its critical composition: (□) $\chi_{\mu 2}$; (■) $\chi_{\mu 2h}$; (◆) $\chi_{\mu 2s}$

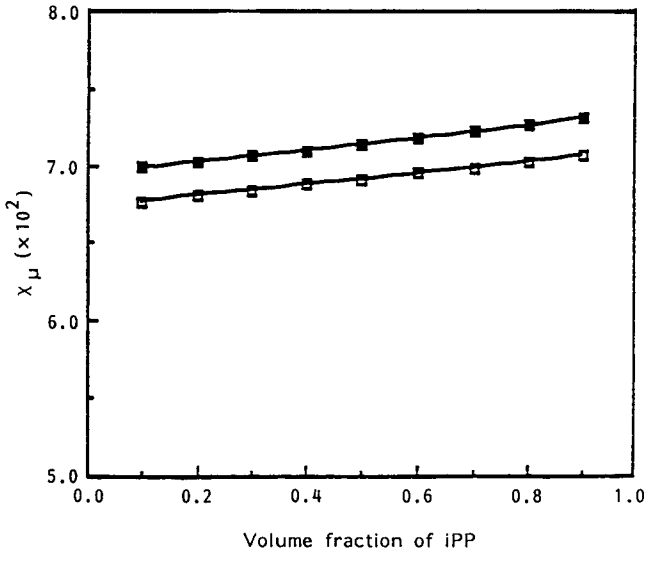

Figure 10 Composition dependence of the interaction parameter of the iPP/TA system at 450 K: (□) $\chi_{\mu 1}$; (■) $\chi_{\mu 2}$

Composition dependence of the interaction parameter

The composition dependence of the interaction parameter for the iPP/TA system is illustrated in *Figures 8* and *10*. As shown in *Figure 10*, the interaction parameter is only slightly composition dependent, and $\chi_{\mu 1}$ and $\chi_{\mu 2}$ are approximately equal near the equilibrium melting temperature of iPP in the iPP/TA mixture (450 K). In *Figure 8*, with increasing temperature the difference between $\chi_{\mu 1}$ and $\chi_{\mu 2}$ decreased, which means a decrease in composition dependence of the interaction parameter.

PHASE DIAGRAM ESTIMATION

Spinodal curve estimation

The spinodal curve is the boundary between the metastable and the unstable regions. The conditions for the spinodal point were described in equation (3). Equations (14)–(16) are substituted into equation (3) to find the spinodal compositions (ϕ'_{2s} and ϕ''_{2s}) at a certain temperature. There are two spinodal points at each temperature, and the locus of these points at various temperatures comprise the spinodal curve shown in *Figure 11*. The shape of the spinodal curve for polymer/diluent system is far from symmetrical due to the size difference between the polymer and the diluent. The spinodal curve is skewed to the diluent side and the critical point (T_c, ϕ_{2c}) is located at a low polymer concentration[17]. The critical temperature for the iPP/TA system was estimated as 429 K, and the critical composition was $\phi_2 = 0.08$, which is exactly the same as that listed in *Table 2*. The critical composition estimated by EOS, where the composition dependence of the interaction parameter was considered, is exactly the same as that calculated by equation (21) to the second decimal place, where the composition dependence is neglected. Therefore, the interaction parameter of the iPP/TA system has little composition dependence.

Binodal curve estimation

Estimation of binodal points by the EOS is not as simple as estimation of the spinodal points. There are two binodal points at each temperature: one at the polymer-lean phase (ϕ'_{2b}) and the other at the polymer-rich phase (ϕ''_{2b}). They were estimated by a graphical method to satisfy the conditions of having a common tangent as shown in equations (4) and (5)[12,13].

At each temperature ϕ'_{2b} and ϕ''_{2b} were calculated from the intersection of the plot of $\partial(\Delta G^1/RT)/\partial\phi_2$ *versus* $(\Delta G^1/RT) - [\partial(\Delta G^1/RT)/\partial\phi_2]\phi_2$ for the polymer lean- and polymer-rich phase regions. A typical plot to find the binodal points is shown in *Figure 12* at 393 K. Similar plots at the other temperatures are shown in reference 44. Thus, estimated binodal points at the various temperatures formed the binodal curve shown in *Figure 11*. The binodal curve meets the spinodal curve at the critical point.

Comparison of estimated and experimental phase diagrams

As discussed earlier, the experimental cloud point should be close to the binodal point. In *Figure 13* the estimated binodal curve is located below the cloud point curve, which was caused by the underestimation of $\chi_{\mu 2}$. The X_{12} parameter was not accurately extrapolated to the polymeric system, which resulted in the underestimation of X_{12} and $\chi_{\mu 2}$. Hydrogen bonding also affected X_{12} and $\chi_{\mu 2}$. Therefore, had the X_{12} parameter been more accurately determined, the estimated binodal curve would more closely agree with the experimental cloud point curve.

As discussed earlier, the cloud points for the polymer-lean phase were hard to determine due to the difficulties in sample preparation. They can be exactly estimated by EOS as proposed in this work if the X_{12} parameter was more accurately determined. The cloud point curve was suspended to the right of the monotectic point by iPP crystallization. However, if the sample was quenched below the monotectic temperature, phase separation is

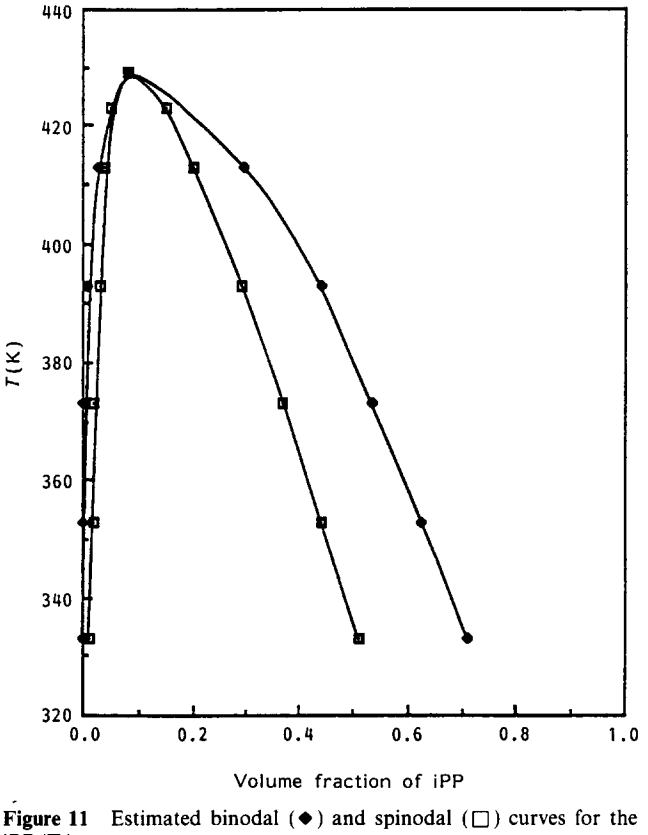

Figure 11 Estimated binodal (◆) and spinodal (□) curves for the iPP/TA system

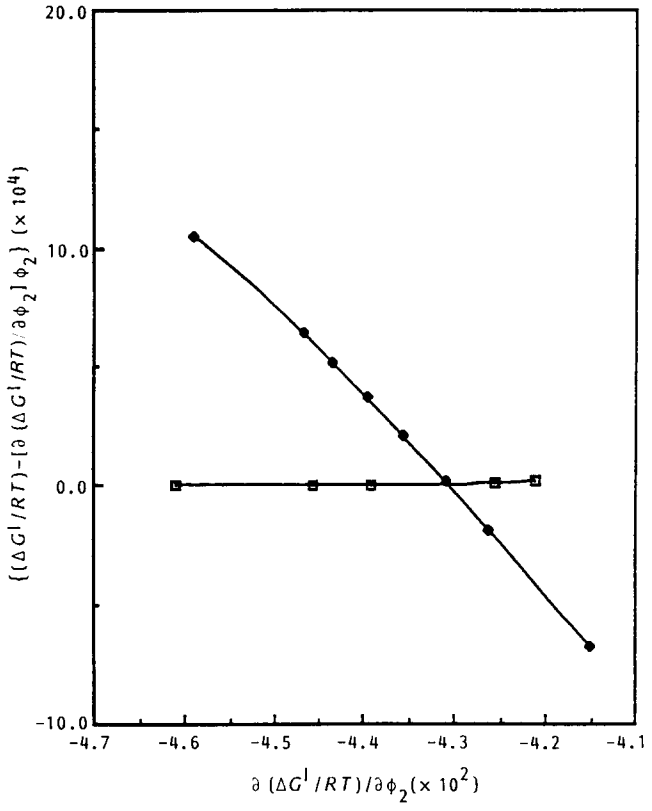

Figure 12 Typical binodal point estimation plot of the iPP/TA system (at 393 K): (□) polymer-lean phase; (◆) polymer-rich phase

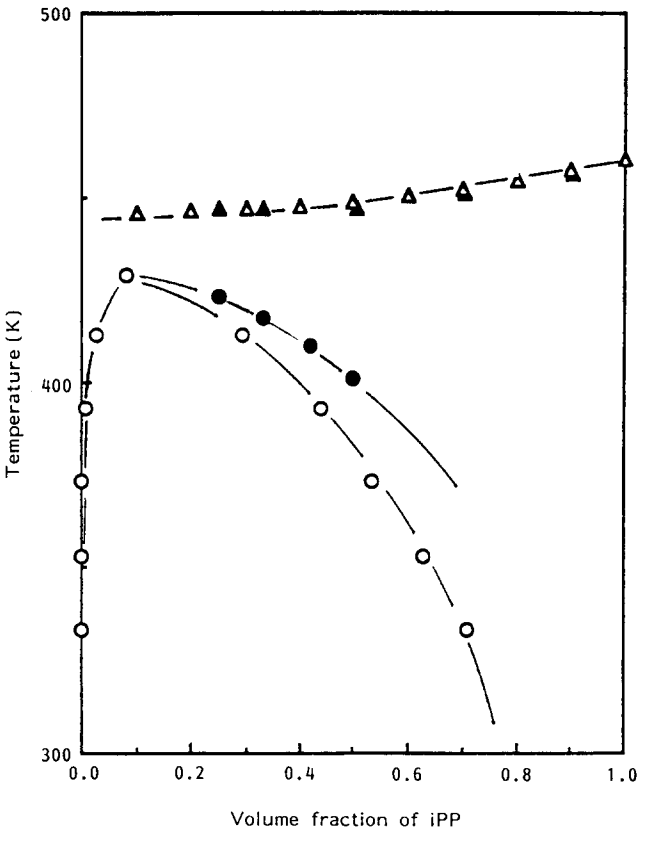

Figure 13 Comparison of experimental and estimated phase diagrams for the iPP/TA system: (▲) experimental equilibrium T_m; (△) equilibrium T_m from EOS; (●) experimental cloud point; (○) binodal point from EOS

governed by the cloud point curve as extended beyond the monotectic point as well as the equilibrium melting curve. The extended cloud point curve, which is impossible to measure experimentally, can be estimated by the binodal point estimation method.

The experimental and estimated equilibrium melting temperatures were also compared in *Figure 13*. The decrease in X_{12} due to the decrease in hydrogen bonding with increasing temperature was not considered in this estimation of equilibrium melting temperatures. Since $\chi_{\mu 2}$ was overestimated in the range of equilibrium melting temperatures shown in *Figure 8*, the equilibrium melting temperatures were overestimated in *Figure 13*. Though the experimental equilibrium melting curve was horizontal below $\phi_2 = 0.5$ due to the liquid–liquid phase separation prior to crystallization in the Hoffman–Weeks analysis, the real equilibrium melting temperatures for $\phi_2 \leqslant 0.5$ should be located below the horizontal line. If the X_{12} parameter was more accurately extrapolated to the polymeric system, and the hydrogen bonding effect was properly considered, the estimation of the equilibrium melting curve could be extended to $\phi_2 \leqslant 0.5$. Therefore, thermodynamic estimation can overcome the experimental limitations.

THERMODYNAMIC STABILITY OF THE SYSTEM

$\Delta G^1/RT$s at various compositions and temperatures were estimated by equations (8)–(10). As shown in *Figure 14*, $\Delta G^1/RT$ decreased with increasing temperature, which means the system became more miscible with increasing temperature. The most important feature of *Figure 14* is that the plot at low temperature is concave at lower

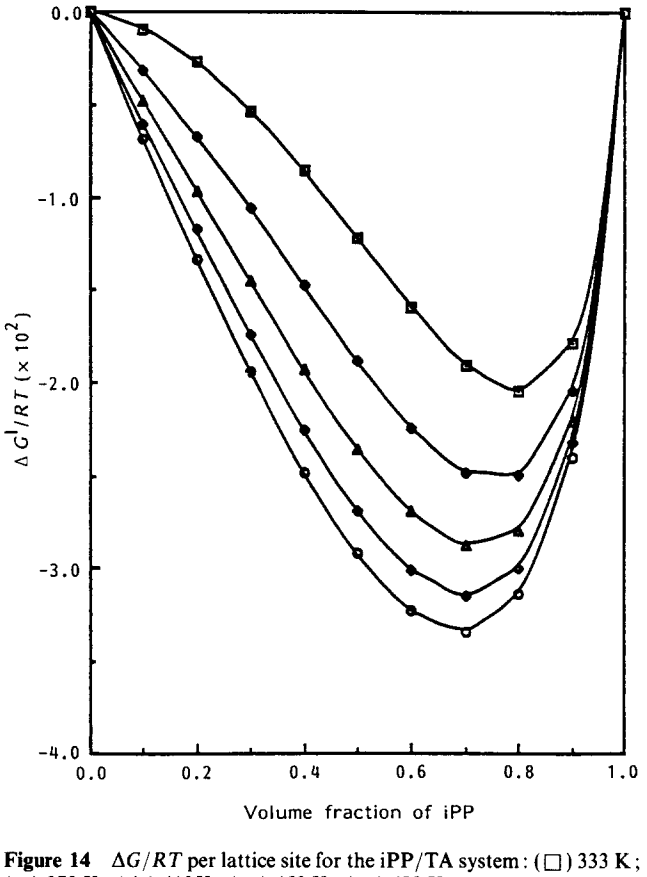

Figure 14 $\Delta G/RT$ per lattice site for the iPP/TA system: (□) 333 K; (◆) 373 K; (△) 413 K; (◇) 453 K; (○) 493 K

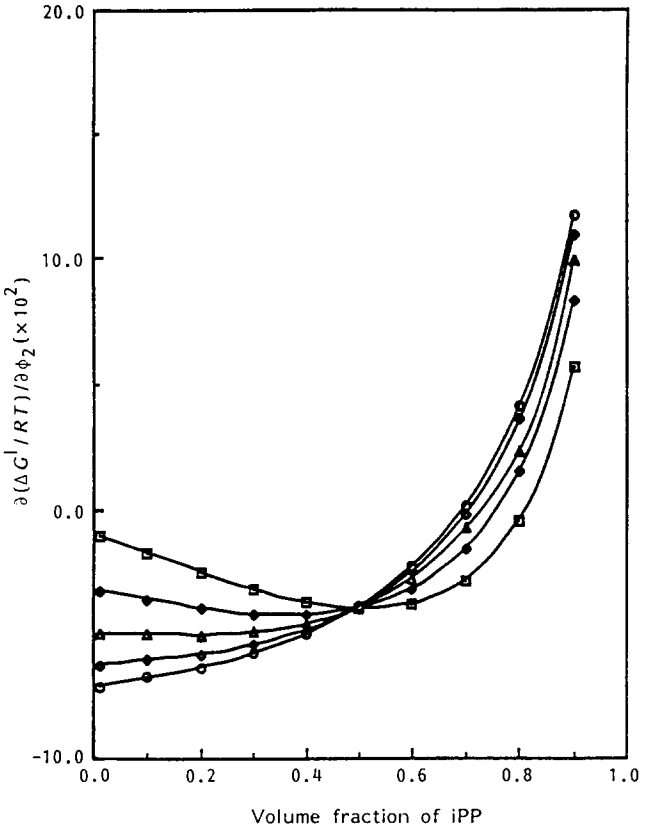

Figure 15 First derivative of $\Delta G/RT$ per lattice site for the iPP/TA system. Symbols as in *Figure 14*

polymer concentrations. The composition range of this shape decreased with increasing temperature and became convex at high temperatures. The region where the curve was concave corresponds to the unstable or spinodal region. Therefore, it was illustrated that the iPP/TA system is unstable at low temperature and low iPP concentration.

$\partial(\Delta G^1/RT)/\partial\phi_2$ was estimated using equations (11) and (12). In *Figure 15*, at low temperatures the derivative decreased with increasing iPP concentration at low iPP concentrations and then increased with increasing iPP concentration. At high temperatures the derivative increased monotonically. The points at which the conditions stated by equations (4) and (5) were satisfied could be found on the low temperatures plots, which decrease and then increase with increasing iPP concentration. These points were the binodal points as obtained in *Figure 12*. There is no way to find these points on the monotonically increasing plots, such as high temperature plots of the iPP/TA system. Therefore, the presence of a metastable region was confirmed for the iPP/TA system.

$\partial^2(\Delta G^1/RT)/\partial\phi_2^2$ was estimated using equations (14) and (15). This is an important plot for determining the spinodal points of the iPP/TA system. At every temperature in *Figure 16*, the second derivative showed a minimum. For convenience a horizontal line was drawn at $\partial^2(\Delta G^1/RT)/\partial\phi_2^2 = 0$, which is a limit for miscibility. At low temperatures much of the plot is less than zero, and the portion less than zero decreased with increasing temperature. At higher temperatures all of the values are positive, which means the system is stable at all compositions. The intersection of the $\partial^2(\Delta G^1/RT)/\partial\phi_2^2$ plot and the horizontal line represents the spinodal points. Between these points, $\partial^2(\Delta G^1/RT)/\partial\phi_2^2$ is negative and the system is unstable. $\partial^2(\Delta G^1/RT)/\partial\phi_2^2$ is a tangent to the horizontal line at 429 K, and the tangential point is the *UCST* of the iPP/TA system. The critical composition was obtained from this point as $\phi_2 = 0.08$, and 429 K was the critical temperature for the iPP/TA system.

CONCLUSIONS

The liquid–liquid phase separation for the iPP/TA system was revealed by both experimental determination and estimation by Flory's EOS theory. Due to the highly polar end group of TA, enthalpic effects caused liquid–liquid phase separation for low iPP concentration. The free volume effect was similar to those of the systems covered in the second paper in this series. The estimated interaction parameters were in good agreement with experimental ones from the cloud points and melting temperatures. The estimated interaction parameter increased with decreasing temperature and increased slightly with increasing iPP concentration.

The dynamic phase diagram was generated by measuring cloud points and iPP crystallization temperatures at a cooling rate of 10 K min^{-1}. The resulting phase diagram showed a monotectic point at $\phi_2 = 0.60$ and 378 K. The equilibrium phase diagram was generated by measuring cloud points and equilibrium melting temperatures using a Hoffman–Weeks plot. The binodal and spinodal curves as well as the equilibrium melting temperature curve estimated by EOS were in good agreement with the experimentally generated curves. The *UCST* of this system was found at $\phi_2 = 0.08$ and 429 K. The experimentally unavailable region of the cloud point

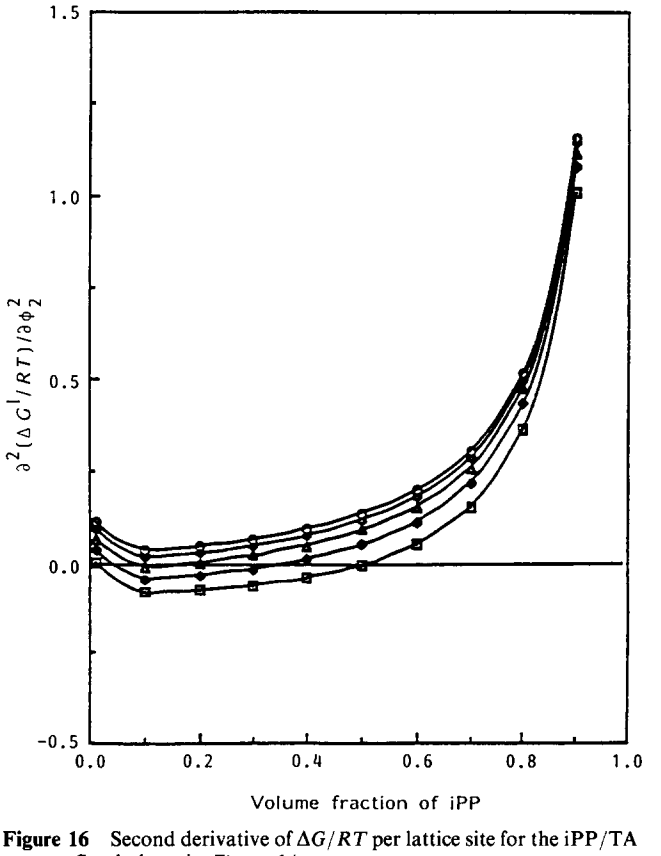

Figure 16 Second derivative of $\Delta G/RT$ per lattice site for the iPP/TA system. Symbols as in *Figure 14*

curve and equilibrium melting temperature curve were estimated by EOS. More accurate extrapolation of the X_{12} parameter to the polymeric system and proper consideration of TA hydrogen bonding effects are required to analyse the system more accurately.

From the information obtained in this paper and the second paper in this series, microporous membrane formation via TIPS can be interpreted and predicted. The knowledge gained in this study and the methodology used to predict the phase diagram can be extended to other polymer/diluent systems without much experimental work.

ACKNOWLEDGEMENTS

The authors gratefully acknowledge the continued generous financial support of the Central Research Technology Development Laboratory of the 3M Company, St. Paul, MN and Texas Advanced Technology Program.

REFERENCES

1 Kim, S. S. and Lloyd, D. R. *Polymer* 1992, **33**, 1036
2 Lloyd, D. R., Kinzer, K. E. and Tseng, H. S. *J. Membr. Sci.* 1990, **52**, 239
3 Lloyd, D. R., Kim, S. S. and Kinzer, K. E. *J. Membr. Sci.* 1991, **64**, 1
4 Kim, S. S. and Lloyd, D. R. *J. Membr. Sci.* 1991, **64**, 13
5 Lim, G. B. A., Kim, S. S., Ye, Q. H., Wang, Y. F. and Lloyd, D. R. *J. Membr. Sci.* 1991, **64**, 31
6 Kim, S. S., Lim, G. B. A., Alwattari, A. A., Wang, Y. F. and Lloyd, D. R. *J. Membr. Sci.* 1991, **64**, 41
7 Alwattari, A. A. and Lloyd, D. R. *J. Membr. Sci.* 1991, **64**, 55
8 Hiatt, W. C., Vitzthum, G. H., Wagener, K. B., Gerlach, K. and Josefiak, C. in 'Materials Science of Synthetic Membranes' (Ed. D. R. Lloyd), ACS Symposium Series No. 269, American Chemical Society, Washington, 1985
9 Kim, S. S. and Lloyd, D. R. *Polymer* submitted
10 Flory, P. J. 'Principles of Polymer Chemistry', Cornell University Press, Ithaca, 1965, pp. 507–576
11 Sanchez, I. C. *Macromolecules* 1978, **11**, 1145
12 Smolders, C. A., van Aartsen, J. J. and Steenbergen, A. *Kolloid-Z. Z. Polym.* 1971, **243**, 14
13 Sanchez, I. C. in 'Encyclopedia of Physical Science and Technology', Vol. XI, Academic Press, New York, 1987, pp. 1–18
14 Cahn, J. W. and Hilliard, J. E. *J. Chem. Phys.* 1958, **28**, 258
15 Cahn, J. W. *Trans. Metall. Soc. AIME* 1968, **242**, 166
16 Nishi, T. and Wang, T. T. *Macromolecules* 1975, **18**, 909
17 Sanchez, I. C. *Polymer* 1989, **30**, 471
18 Rostami, S. and Walsh, D. J. *Macromolecules* 1984, **17**, 315
19 Sham, C. K. and Walsh, D. J. *Polymer* 1987, **28**, 804
20 Hill, R. G., Tomlins, P. E. and Higgins, J. S. *Macromolecules* 1985, **18**, 2555
21 Hill, R. G., Tomlins, P. E. and Higgins, J. S. *Polymer* 1985, **26**, 1708
22 Kumaki, J. and Hashimoto, T. *Macromolecules* 1986, **19**, 763
23 Kyu, J. and Saldanha, J. M. *Macromolecules* 1988, **21**, 1021
24 Derham, K. E., Goldsbrough, J. and Gordon, M. *Pure Appl. Chem.* 1974, **38**, 97
25 Koningsveld, M. and Kleintjens, L. A. *J. Polym. Sci., Polym. Symp.* 1977, **61**, 221
26 Ubrich, L. A., Cheikhlarbi, B. F., Halary, J. L., Monnerie, L., Baurer, B. J. and Han, C. C. *Macromolecules* 1986, **19**, 810
27 Halary, J. L., Ubrich, J. M., Nunzi, J. M., Monnerie, L. and Stein, R. S. *Polymer* 1984, **25**, 956
28 Caneba, G. T. and Soong, D. S. *Macromolecules* 1985, **18**, 2538
29 Caneba, G. T. and Soong, D. S. *Macromolecules* 1985, **18**, 2545
30 Tsai, F.-j. and Torkelson, J. M. *Macromolecules* 1990, **23**, 775
31 Russel, T. P., Hadziioannous, G. and Warburton, W. K. *Macromolecules* 1985, **18**, 78
32 Tsai, F.-j. and Torkelson, J. M. *Macromolecules* 1988, **21**, 1026
33 Higgins, J. S., Fruitwala, H. and Tomlins, P. E. *Macromolecules* 1989, **22**, 3674
34 Lim, G. B. A. *PhD Dissertation* The University of Texas at Austin, 1990
35 Mandelkern, L., Smith, F. C. and Cahn, E. K. *Macromolecules* 1989, **22**, 2663
36 Hoffman, J. D. and Weeks, J. J. *J. Res. Natl Bur. Stand.* 1962, **66**, 13
37 Painter, P. C., Park, Y. and Coleman, M. M. *Macromolecules* 1989, **22**, 570
38 Eichinger, B. E. and Flory, P. J. *Trans. Faraday Soc.* 1968, **64**, 2035, 2053, 2961, 2066
39 Patterson, D. and Robard, A. *Macromolecules* 1978, **11**, 690
40 Vinogradov, S. N. and Linnell, R. H. 'Hydrogen Bonding', Van Nostrand Reinhold Company, New York, 1971, pp. 114–146
41 Painter, P. C., Park, Y. and Coleman, M. M. *Macromolecules* 1989, **22**, 580
42 Painter, P. C., Park, Y. and Coleman, M. M. *Macromolecules* 1989, **22**, 586
43 Lee, J. Y., Painter, P. C. and Coleman, M. M. *Macromolecules* 1988, **21**, 346
44 Kim, S. S. *PhD Dissertation* The University of Texas at Austin, 1990